Electronic Supplementary Material (ESI) for Dalton Transactions.
This journal is © The Royal Society of Chemistry 2024

Electronic Supplementary Information for:

Cerium(III) and 5-methylisophthalate based MOFs with slow relaxation of the magnetization and photoluminescent emission

Oier Pajuelo-Corral,[a] MCarmen Contreras,[b] Sara Rojas,[b] Duane Choquesillo-Lazarte,[c] José M. Seco,[a] Antonio Rodríguez-Diéguez,[b] Alfonso Salinas-Castillo,[d] Javier Cepeda,[a,*] Andoni Zabala-Lekuona[a,*] and Iñigo J. Vitorica-Yrezabal[b,*]

[a.] *Departamento de Química Aplicada, Facultad de Química, Universidad del País Vasco/Euskal Herriko Unibertsitatea (UPV/EHU), 20018, Donostia, Spain*
[b.] *Departamento de Química Inorgánica, Facultad de Ciencias, Universidad de Granada, 18071, Granada, Spain; vitorica@ugr.es*
[c.] *Laboratorio de Estudios Cristalograficos, IACT, CSIC-Universidad de Granada, Av. De las palmeras 4, Armilla, Granada E-18100, Spain*
[d.] *Departamento de Química Analítica, Facultad de Humanidades, Universidad de Granada, 18071, Granada, Spain*

Contents:

S1. Continuous Shape Measurements (CShM).

Table S1.- Continuous Shape Measurements for the Ce(III) coordination environment in compounds **GR-MOF-17**and **GR-MOF-18**.

EP-9	1 D9h	Enneagon
OPY-9	2 C8v	Octagonal pyramid
HBPY-9	3 D7h	Heptagonal bipyramid
JTC-9	4 C3v	Johnson triangular cupola J3
JCCU-9	5 C4v	Capped cube J8
CCU-9	6 C4v	Spherical-relaxed capped cube
JCSAPR-9	7 C4v	Capped square antiprism J10
CSAPR-9	8 C4v	Spherical capped square antiprism
JTCTPR-9	9 D3h	Tricapped trigonal prism J51
TCTPR-9	10 D3h	Spherical tricapped trigonal prism
JTDIC-9	11 C3v	Tridiminished icosahedron J63
HH-9	12 C2v	Hula-hoop
MFF-9	13 Cs	Muffin

Structure [ML9]	**EP-9**	**OPY-9**	**HBPY-9**	**JTC-9**	**JCCU-9**	**CCU-9**	**JCSAPR-9**
Ce1 (GR-MOF-17)	32.675	21.981	17.313	15.281	9.644	8.578	3.752
Ce1 (GR-MOF-18)	34.150	21.407	14.443	16.258	10.717	8.332	5.850

Structure [ML9]	**CSAPR-9**	**JTCTPR-9**	**TCTPR-9**	**JTDIC-9**	**HH-9**	**MFF-9**
Ce1 (GR-MOF-17)	2.861	5.511	3.316	12.033	8.300	**2.042**
Ce1 (GR-MOF-18)	4.361	7.313	4.704	14.311	6.432	**2.754**

S2. Crystallographic parameters and selected bond lengths and angles

Table S2. Single crystal X-ray diffraction data and structure refinement details of compounds **GR-MOF-17** and **GR-MOF-18**.

Compound	**GR-MOF-17**	**GR-MOF-18**
Empirical formula	$C_{18}H_{13}CeO_8$	$C_{12}H_{13}CeClNO_5$
Formula weight	497.40	426.80
Temperature/K	285.00	100
Crystal system	orthorhombic	orthorhombic
Space group	$P2_12_12_1$	$Pna2_1$
a/Å	7.9985(14)	18.2385(11)
b/Å	12.628(2)	9.7448(5)
c/Å	16.058(3)	7.8405(4)
α/°	90	90
β/°	90	90
γ/°	90	90
Volume/Å^3	1621.9(5)	1393.50(13)
Z	4	4
ρ_{calc}g/cm^3	2.037	2.034
μ/mm^{-1}	2.855	3.475
F(000)	972.0	828.0
Crystal size/mm^3	0.08 × 0.08 × 0.07	0.07 × 0.04 × 0.04
Radiation	MoKα (λ = 0.71073)	MoKα (λ = 0.71073)
2Θ range for data collection/°	5.074 to 55.02	6.118 to 54.988
Index ranges	-10 ≤ h ≤ 9, -16 ≤ k ≤ 16, -20 ≤ l	-23 ≤ h ≤ 20, -12 ≤ k ≤ 12, -9 ≤ l ≤ 10
Reflections collected	28766	15449
Independent reflections	3723 [R_{int} = 0.0432, R_{sigma} = 0.0301]	3098 [R_{int} = 0.0250, R_{sigma} = 0.0247]
Data/restraints/parameters	3723/0/247	3098/1/185
Goodness-of-fit on F^2	1.076	1.090
Final R indexes [I>=2σ (I)]	R_1 = 0.0159, wR_2 = 0.0392	R_1 = 0.0161, wR_2 = 0.0376
Final R indexes [all data]	R_1 = 0.0163, wR_2 = 0.0396	R_1 = 0.0198, wR_2 = 0.0395
Largest diff. peak/hole / e Å^{-3}	0.46/-0.56	0.78/-0.26
Flack parameter	0.006(6)	0.001(16)

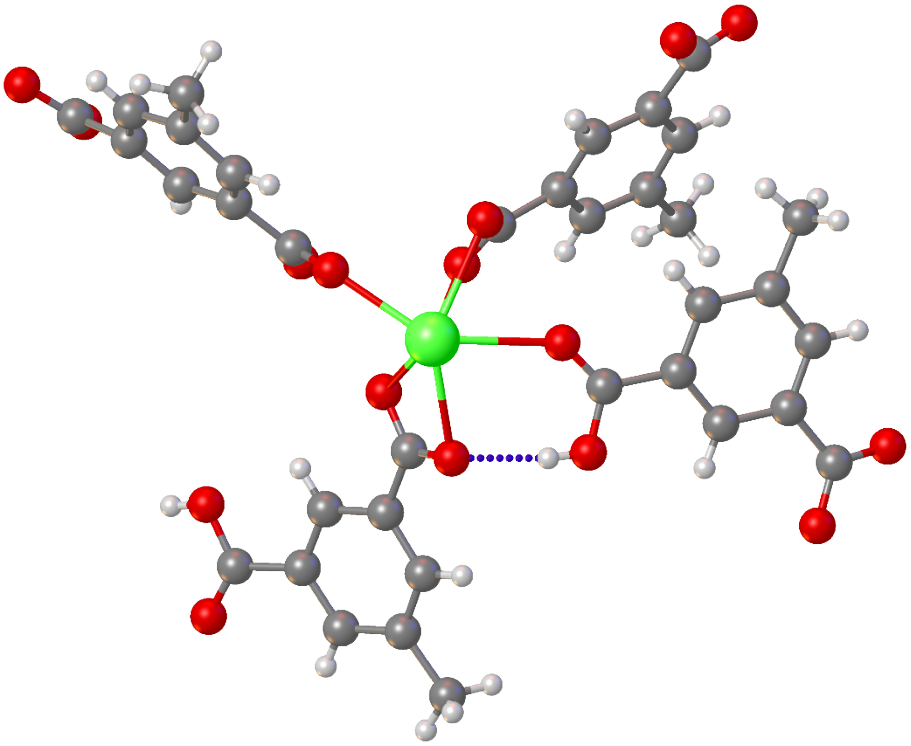

Figure S1. Hydrogen bond between the carboxylate and carboxylic acid groups in crystal structure **GR-MOF17**. Cerium in green, oxygens in red carbons in grey and hydrogens in white. Hydrogen bond in dash blue line.

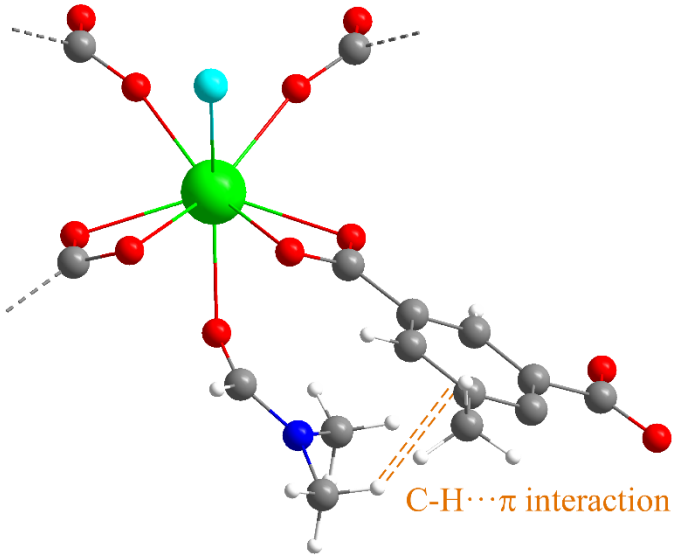

Figure S2. Excerpt of the framework showing the interaction between the coordinated DMF and 5Meip ligands in compound **GR-MOF-18**. Atom colour code as Figure S1 with Chloride in clear blue and nitrogen in dark blue.

Table S3. Structural parameters (Å, º) of the C-H···π interaction found in compound **GR-MOF-18**.[a]

X–H···Cg(ring)[b]	H···Cg	H···Perp	γ	X–H···Cg	X···Cg	X–H,π

C–H···5Meip(i)	2.87	2.85	5.48	136	3.632(7)	3.41–3.50

[a] Symmetry: (i) 1/2 + x, -1/2 + y, 1/2 + z. H···Cg: distance of H to ring Cg; H···Perp: perpendicular distance of H to ring plane; γ: angle between Cg-H vector and ring normal. [b] Cg refer to ring centre of gravity; X–H···Cg: X-H-Cg angle (degrees); X···Cg: Distance of X to Cg (Å); X–H,π: Angle of the X-H bond with the π-plane. Ring: C2, C3, C4, C5, C2a, C3a.

Table S4. Crystal structure: selected bond lengths and angles.

GR-MOF-17		**GR-MOF-18**	
Ce1 O1$^{(i)}$	2.517(2)	Ce1 Cl1	2.8940(9)
Ce1 O1	2.700(2)	Ce1 Cl1$^{(ii)}$	2.9164(9)
Ce1 O2	2.594(2)	Ce1 O1$^{(iii)}$	2.677(2)
Ce1 O3	2.415(2)	Ce1 O1	2.499(2)
Ce1 O4$^{(i)}$	2.474(2)	Ce1 O2$^{(iii)}$	2.512(2)
Ce1 O5	2.613(2)	Ce1 O3	2.494(2)
Ce1 O7	2.544(2)	Ce1 O3$^{(iii)}$	2.694(2)
Ce1 O8	2.661(2)	Ce1 O4	2.526(2)
Ce1 O8$^{(i)}$	2.469(2)	Ce1 O5	2.447(2)
Ce1 Ce1$^{(iii)}$	4.2301(7)	Ce1 Ce1$^{(iii)}$	4.0735(2)

Symmetry: (i) 1/2+X,1/2-Y,1-Z; (ii) -2-X,-Y,-1/2+Z; (iii) -2-X,-Y,1/2+Z

S3. Magnetic measurements.

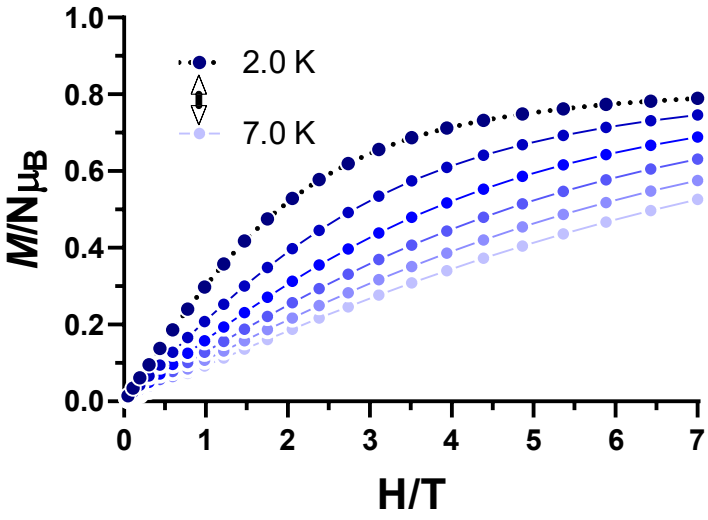

Figure S3. Field dependence of the magnetization in the 2-7 K temperature range for **GR-MOF-17**.

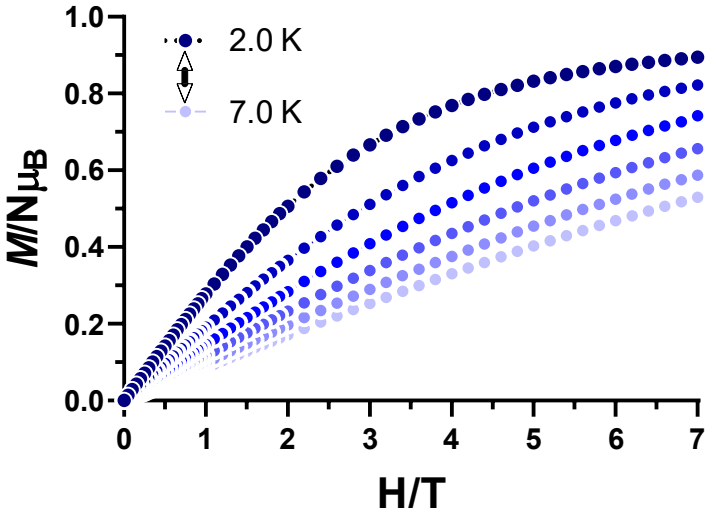

Figure S4. Field dependence of the magnetization in the 2-7 K temperature range for **GR-MOF-18**.

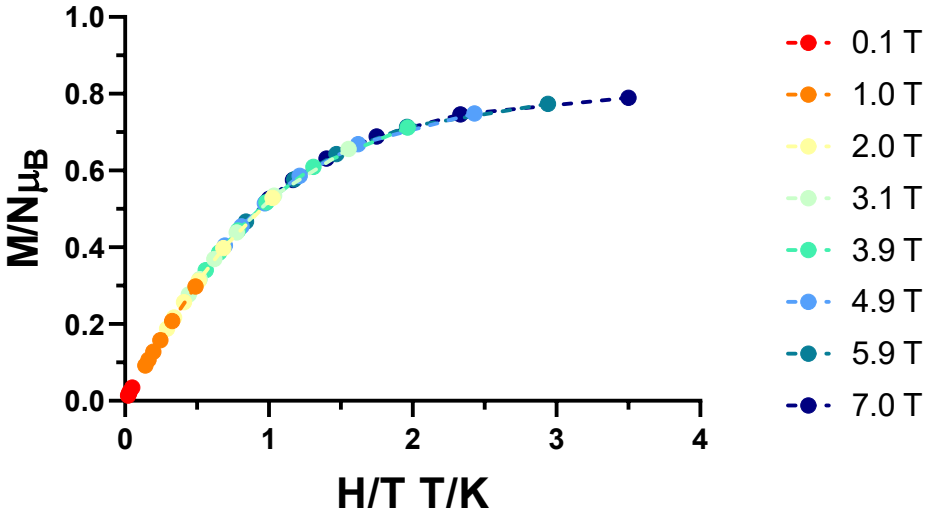

Figure S5. Isothermal reduced magnetization curves in the 2-7 K temperature range for **GR-MOF-17**. Dashed lines are a guide to the eye.

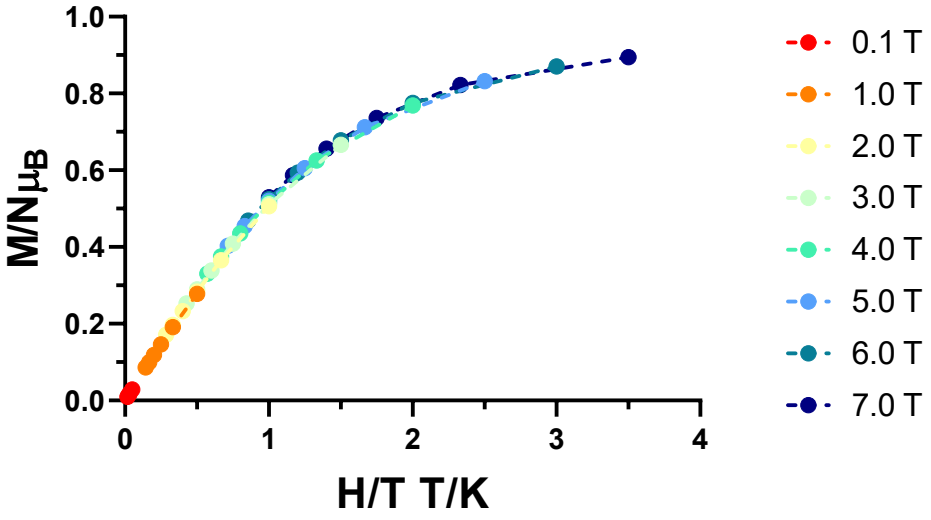

Figure S6. Isothermal reduced magnetization curves in the 2-7 K temperature range for **GR-MOF-18**. Dashed lines are a guide to the eye.

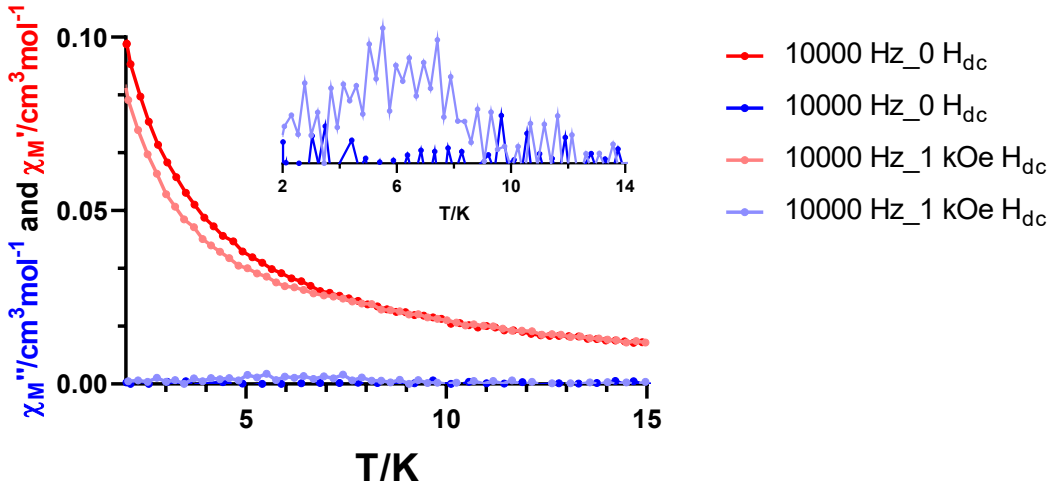

Figure S7. Temperature dependence of the in phase (red) and out-of-phase (blue) components of the *ac* susceptibility in a zero (dark) and 1 kOe (light) *dc* applied field for **GR-MOF-17**.

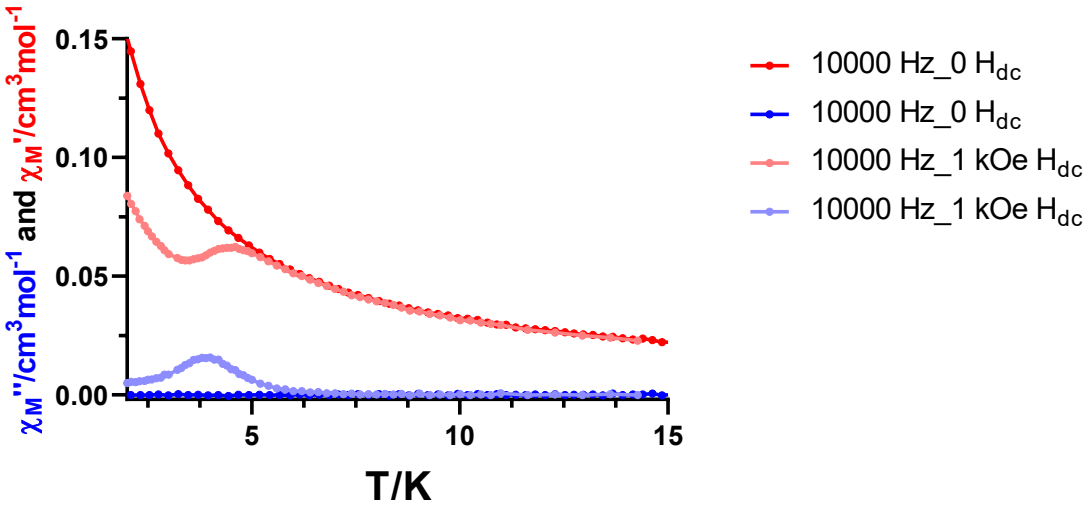

Figure S8. Temperature dependence of the in phase (red) and out-of-phase (blue) components of the *ac* susceptibility in a zero (dark) and 1 kOe (light) *dc* applied field for **GR-MOF-18**.

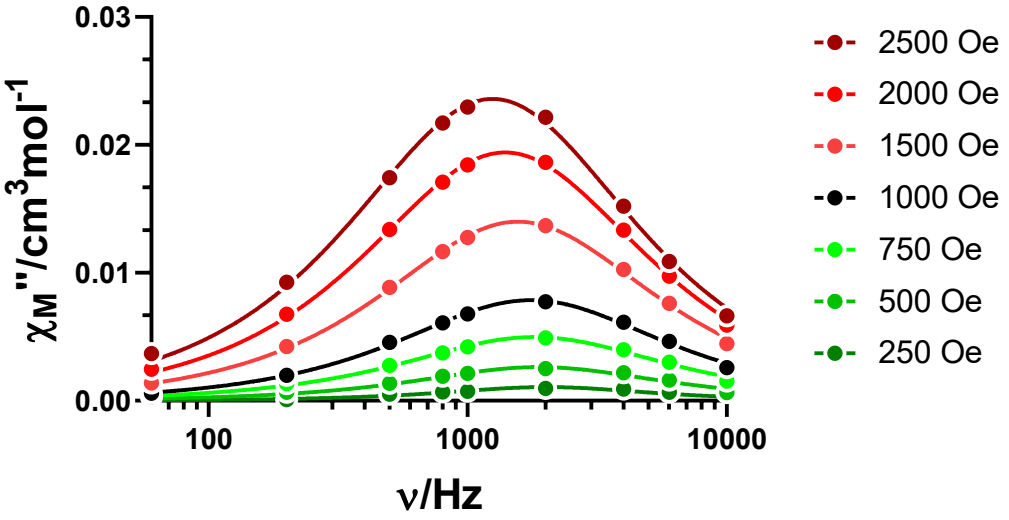

Figure S9. Field dependence of the out-of-phase signal *vs* frequency at 4.0 K for **GR-MOF-17**.

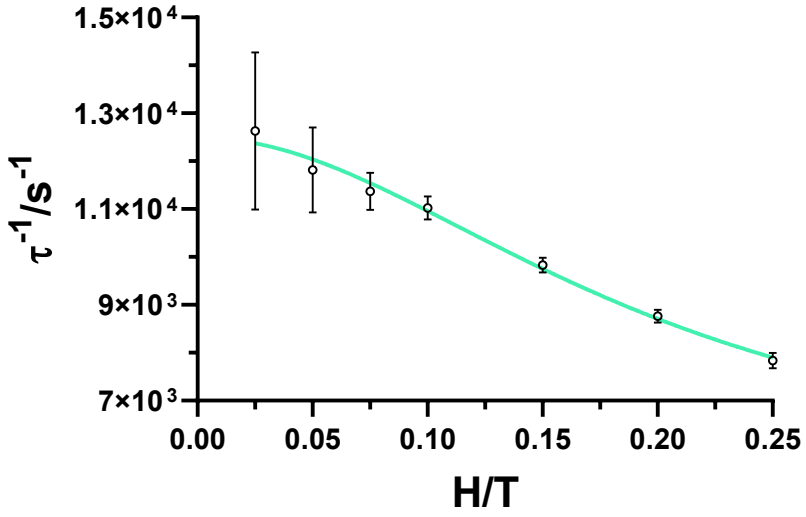

Figure S10. The inverse of the relaxation times obtained at different magnetic fields at 4.0 K for **GR-MOF-17**. The fit (turquoise line) corresponds to the fitting considering the Raman process in equation 1 (manuscript).

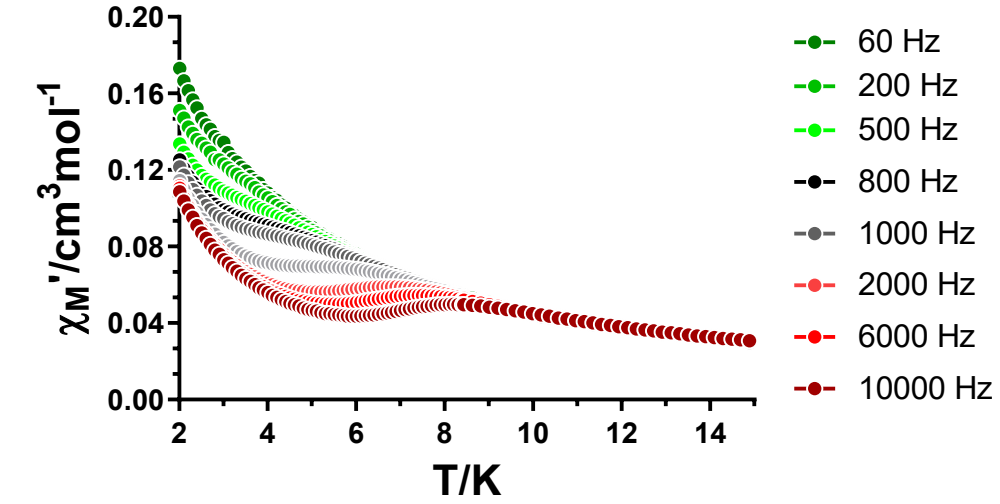

Figure S11. Temperature dependence of the in-phase components of the *ac* susceptibility in a *dc* applied field of 2.5 kOe for **GR-MOF-17**.

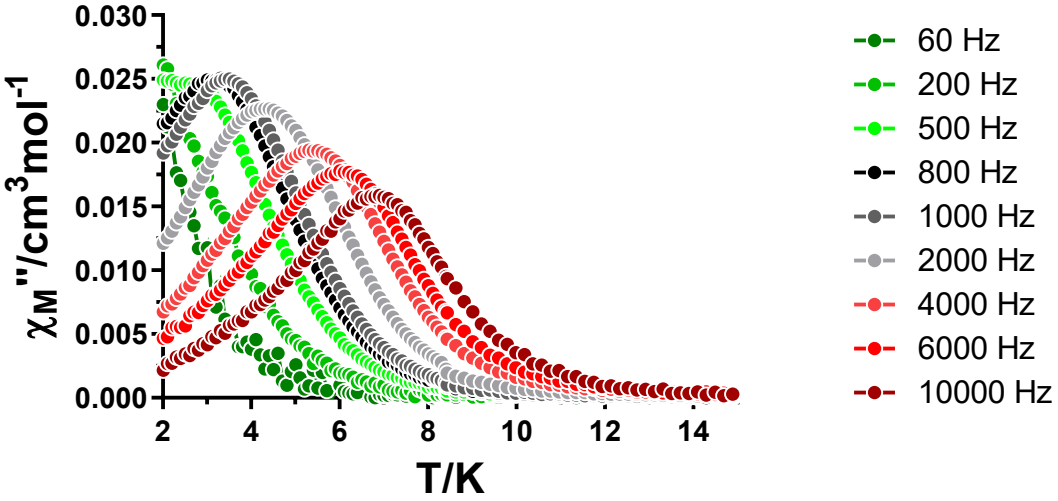

Figure S12. Temperature dependence of the out-of-phase components of the *ac* susceptibility in a *dc* applied field of 2.5 kOe for **GR-MOF-17**.

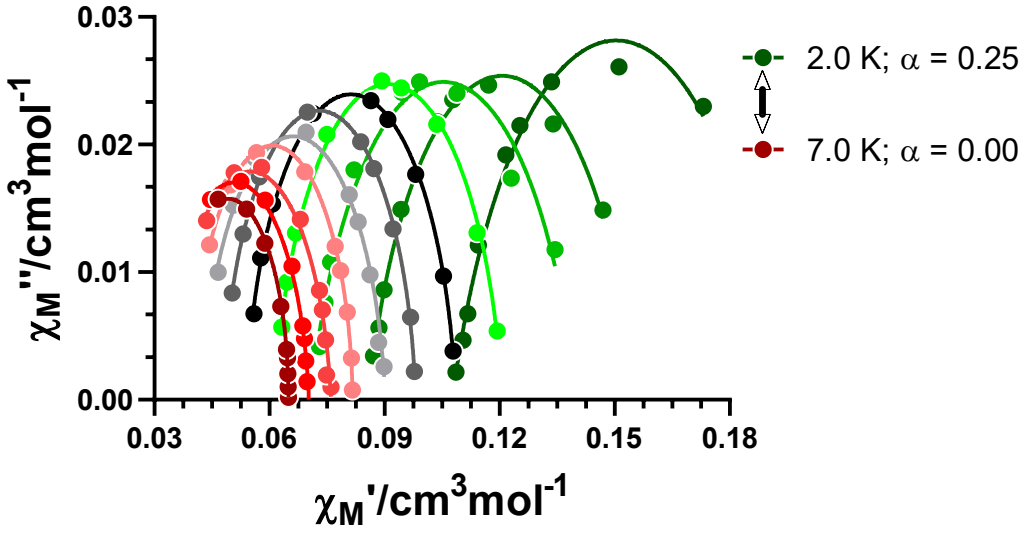

Figure S13. Cole-Cole plots under 2.5 kOe field for **GR-MOF-17**. Solid lines represent the best fit to the generalized Debye model.

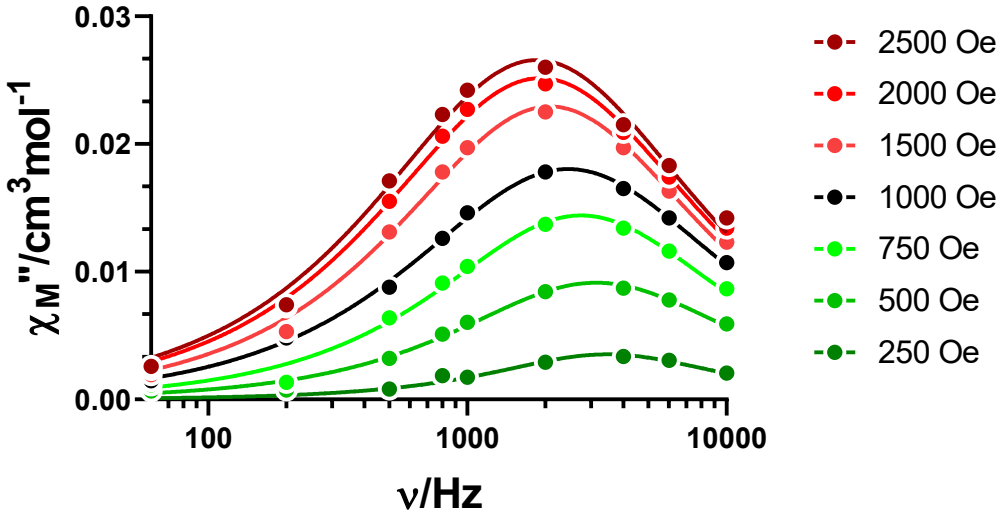

Figure S14. Field dependence of the out-of-phase signal *vs* frequency at 3.2 K for **GR-MOF-18**.

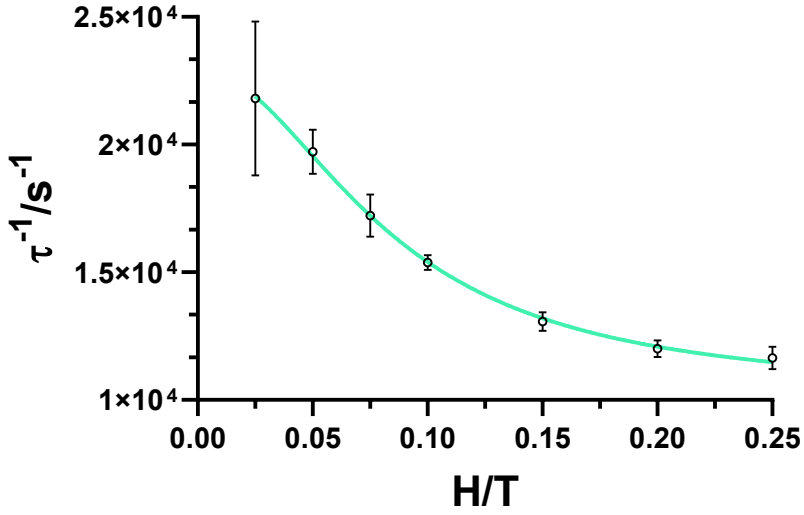

Figure S15. The inverse of the relaxation times obtained at different magnetic fields at 3.2 K for **GR-MOF-18**. The fit (turquoise line) corresponds to the fitting considering the Raman process in equation 1 (manuscript).

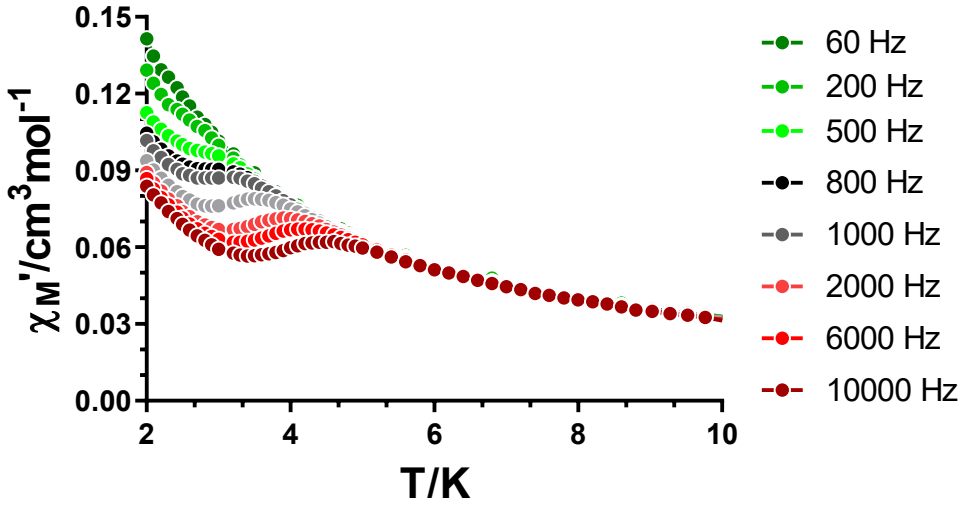

Figure S16. Temperature dependence of the in-phase components of the *ac* susceptibility in a *dc* applied field of 1 kOe for **GR-MOF-18**.

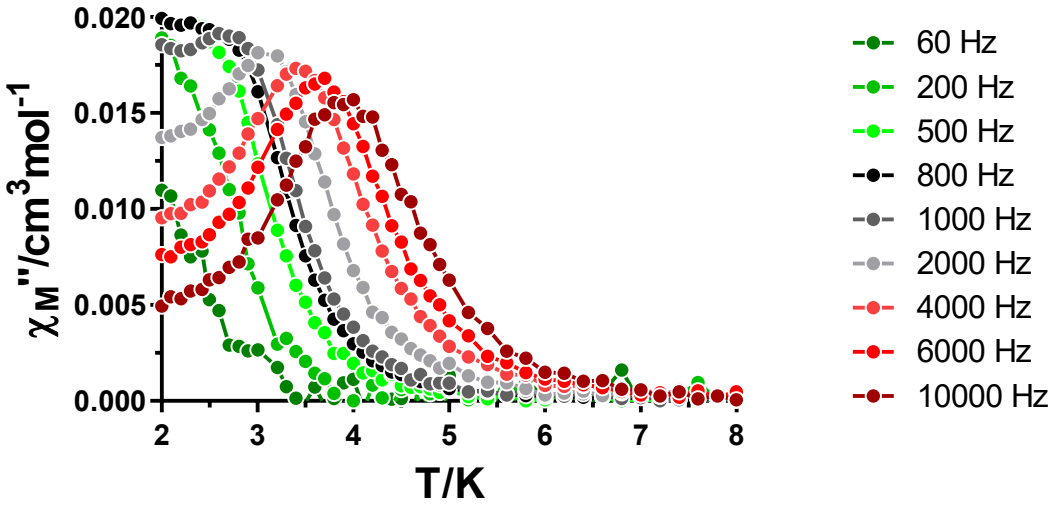

Figure S17. Temperature dependence of the out-of-phase components of the *ac* susceptibility in a *dc* applied field of 1 kOe for **GR-MOF-18**.

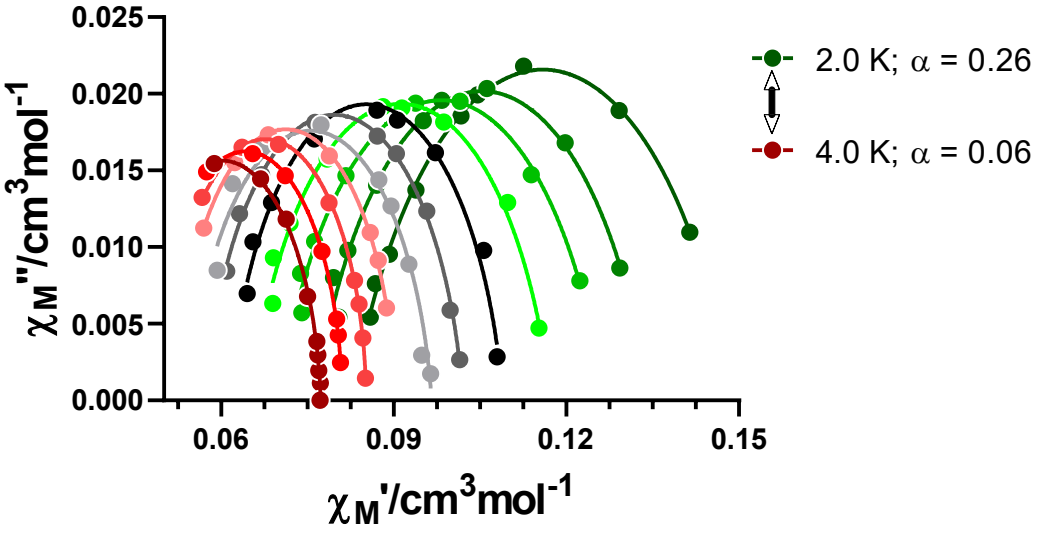

Figure S18. Cole-Cole plots under 1 kOe field for **GR-MOF-18**. Solid lines represent the best fit to the generalized Debye model.

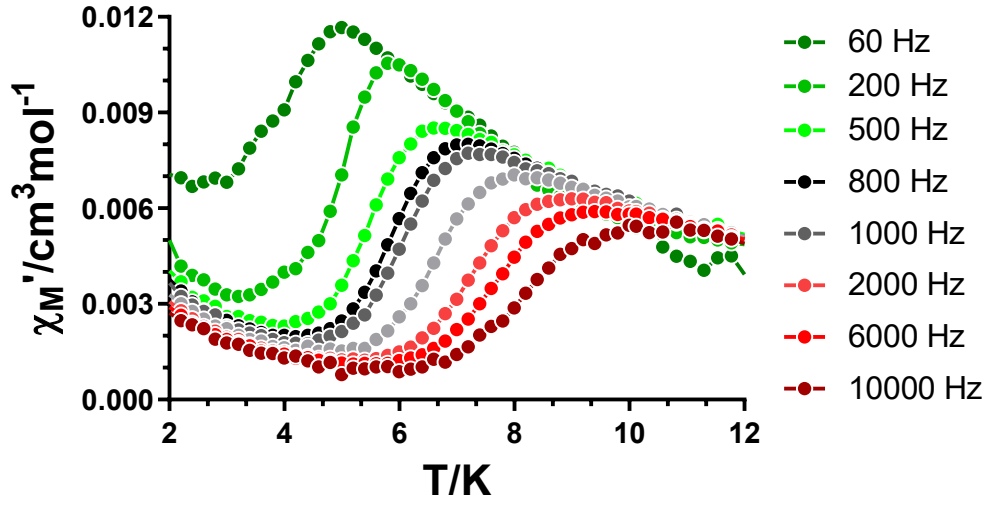

Figure S19. Temperature dependence of the in-phase components of the *ac* susceptibility in a *dc* applied field of 2.5 kOe for **GR-MOF-17@La**.

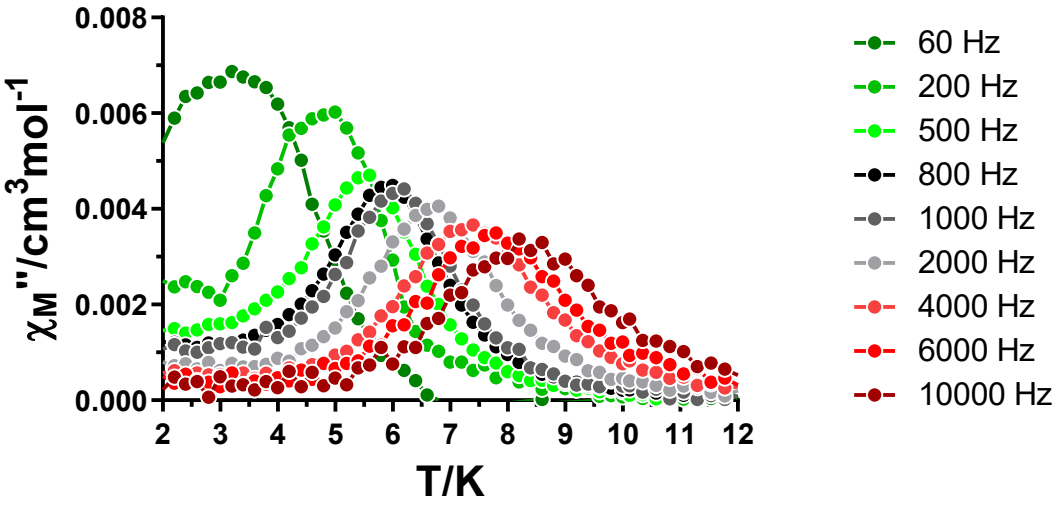

Figure S20. Temperature dependence of the out-of-phase components of the *ac* susceptibility in a *dc* applied field of 2.5 kOe for **GR-MOF-17@La**.

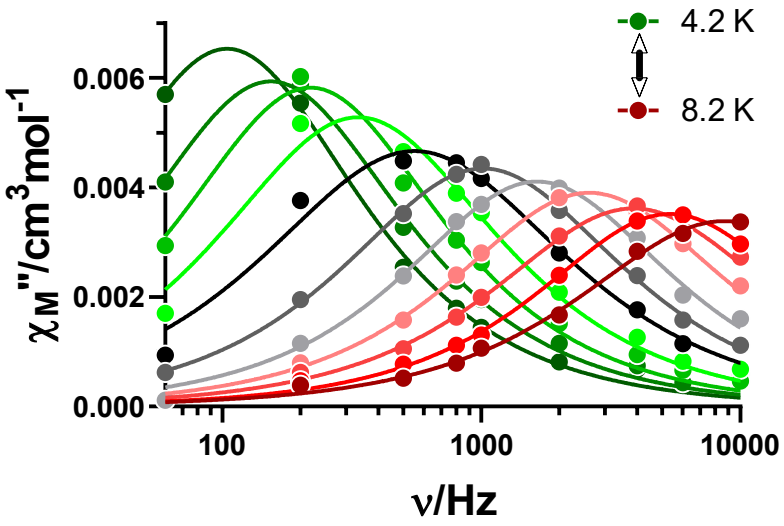

Figure S21. Variable-temperature frequency dependence of the χ_M'' signal under 2.5 kOe applied field for **GR-MOF-17@La**.

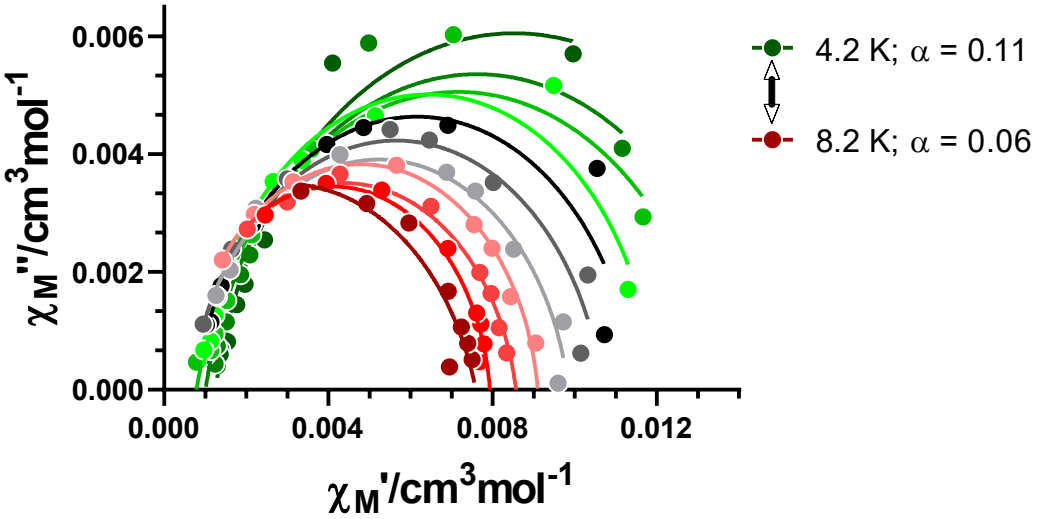

Figure S22. Cole-Cole plots under 2.5 kOe field for **GR-MOF-17@La**. Solid lines represent the best fit to the generalized Debye model.

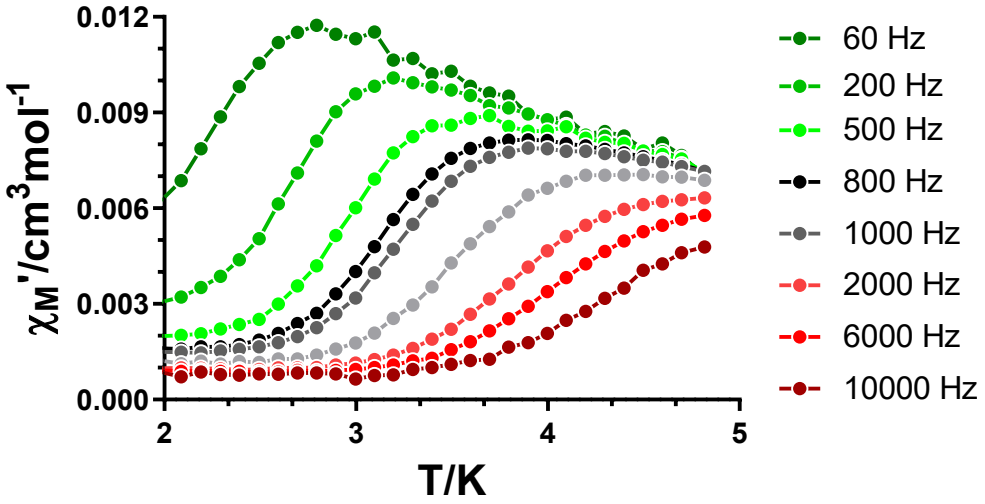

Figure S23. Temperature dependence of the in-phase components of the *ac* susceptibility in a *dc* applied field of 2.5 kOe for **GR-MOF-18@La**.

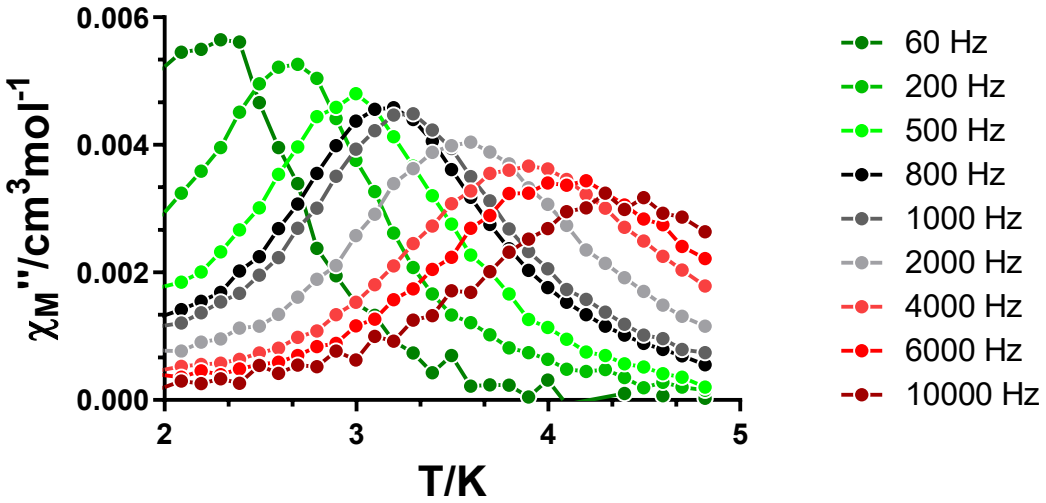

Figure S24. Temperature dependence of the out-of-phase components of the *ac* susceptibility in a *dc* applied field of 2.5 kOe for **GR-MOF-18@La**.

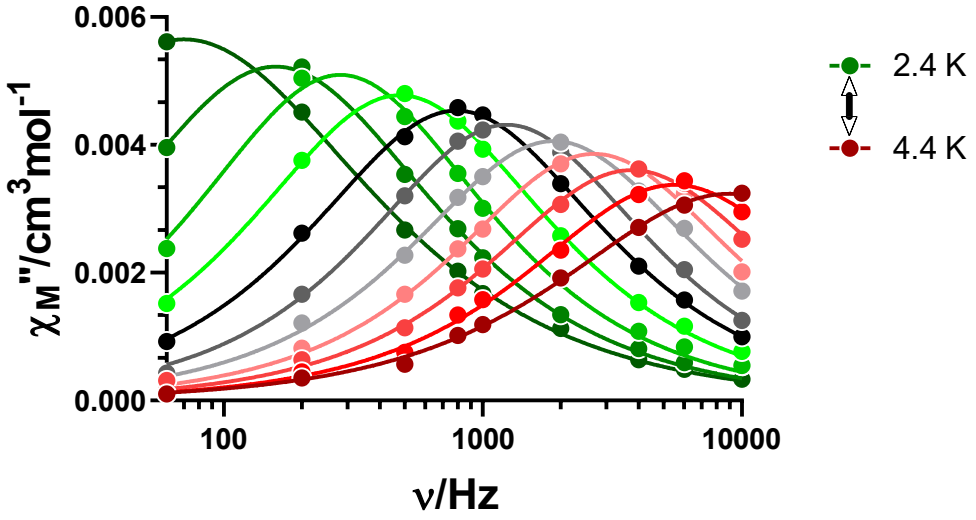

Figure S25. Variable-temperature frequency dependence of the χ_M'' signal under 2.5 kOe applied field for **GR-MOF-18@La**.

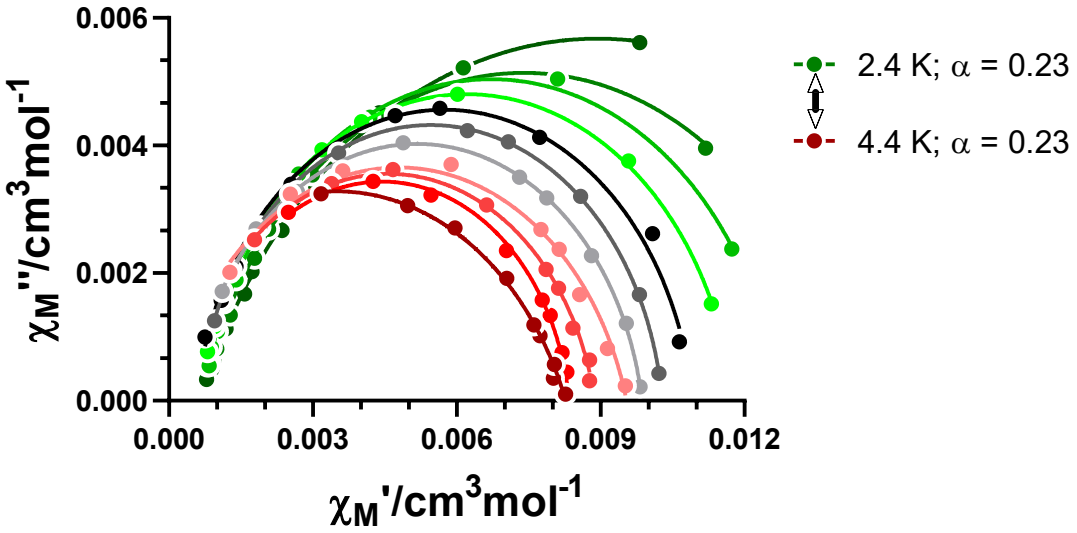

Figure S26. Cole-Cole plots under 2.5 kOe field for **GR-MOF-18@La**. Solid lines represent the best fit to the generalized Debye model.

S4. Computational calculations of magnetic properties.

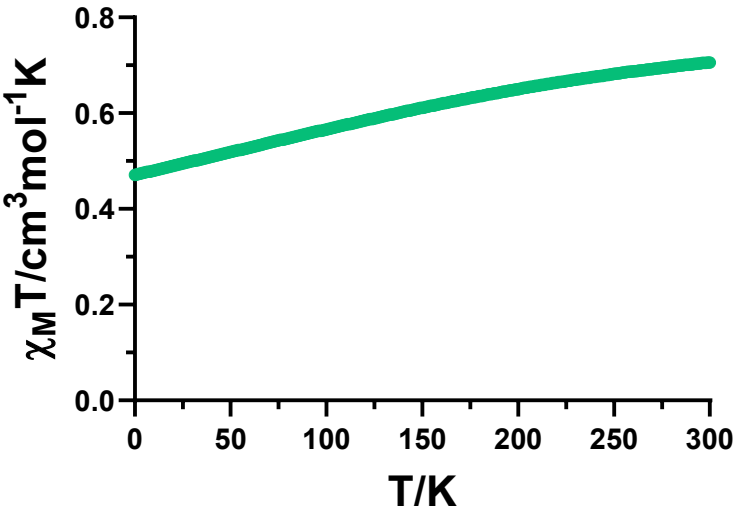

Figure S27. Theoretically calculated variable-temperature dc magnetic susceptibility data for **GR-MOF-17.**

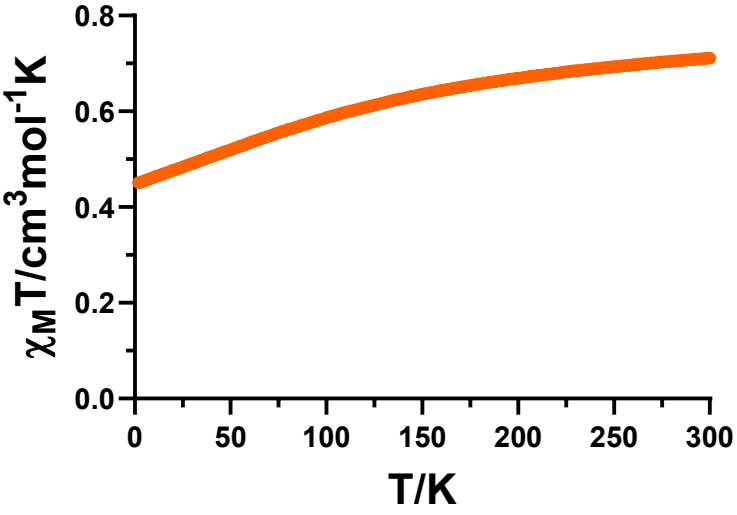

Figure S28. Theoretically calculated variable-temperature dc magnetic susceptibility data for **GR-MOF-18.**

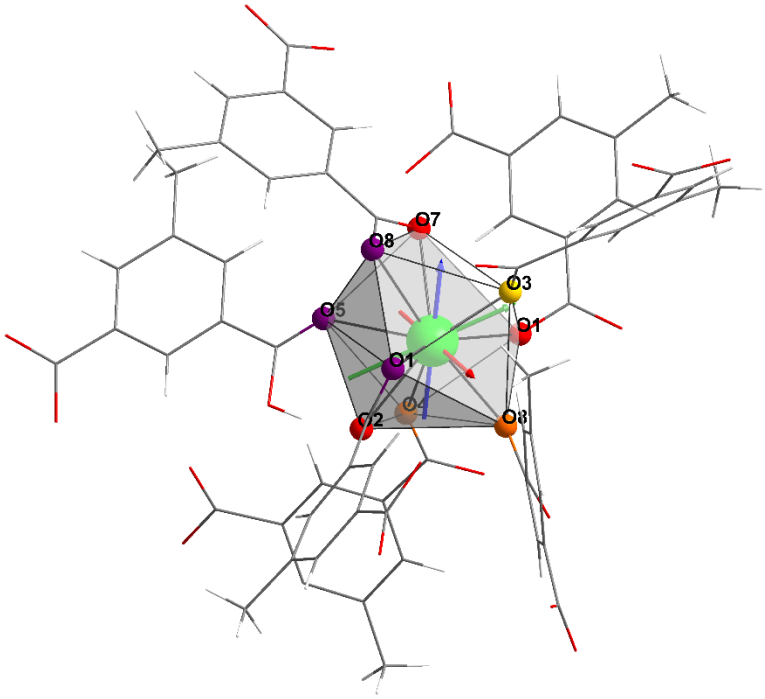

Figure S29. View of the calculated g-tensor for a coordination excerpt of compound **GR-MOF-17**. The shortest Ce-O bond distances are shown by O atoms in light colours (yellow in O3 indicates the shortest distance of 2.415(2) Å and orange in O8(i) and O4 slightly longer distances of 2.469(2) and 2.474(2) Å, respectively. The longest distances (above 2.6 Å) are shown with O atoms in darker purple colour.

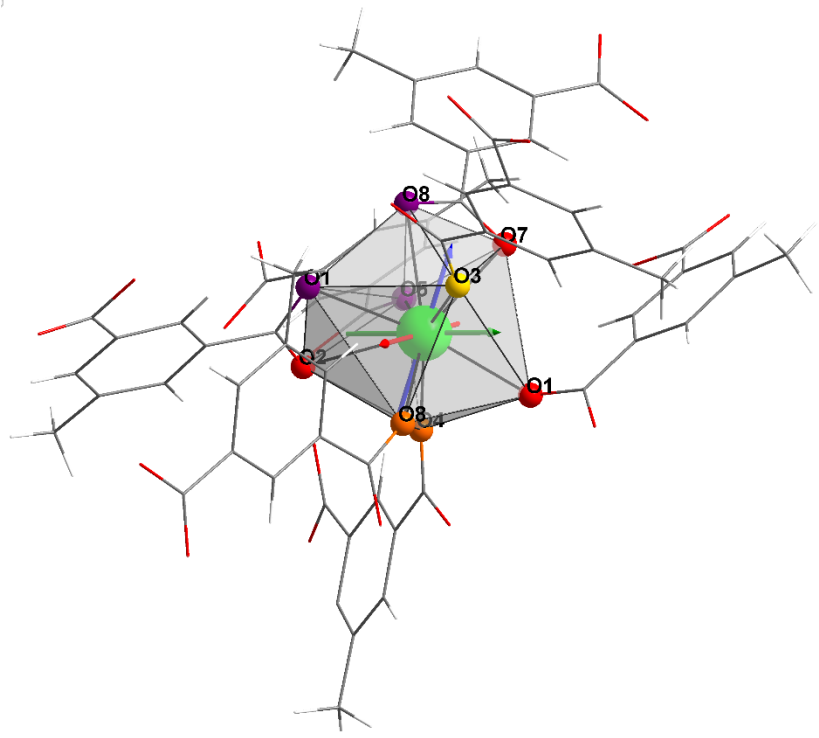

Figure S30. Calculated g-tensor for a coordination excerpt of compound **GR-MOF-17** along a different view to observe how short and large bond distances are not well distributed into appropriate planes. Colour code of atoms is the same as in previous figure.

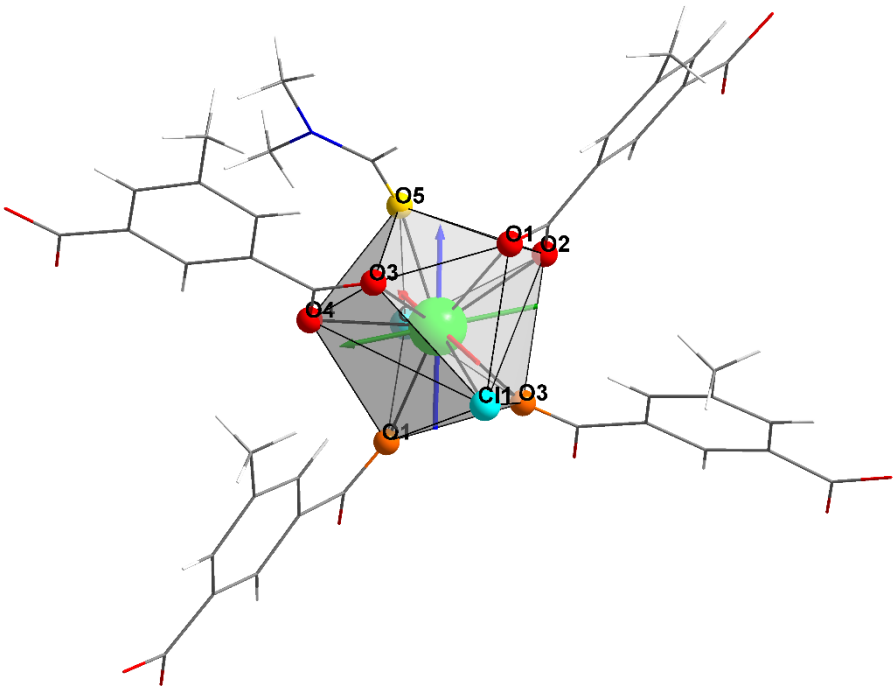

Figure S31. View of the calculated g-tensor for a coordination excerpt of compound **GR-MOF-18**. The shortest Ce-O bond distances are shown by O atoms in light colours (yellow in O5 indicates the shortest distance of 2.447(2) Å and orange in O3 and O1 slightly longer distances of 2.494(2) and 2.499(2) Å, respectively. The longest distances (above 2.89 Å) correspond to Cl ligands.

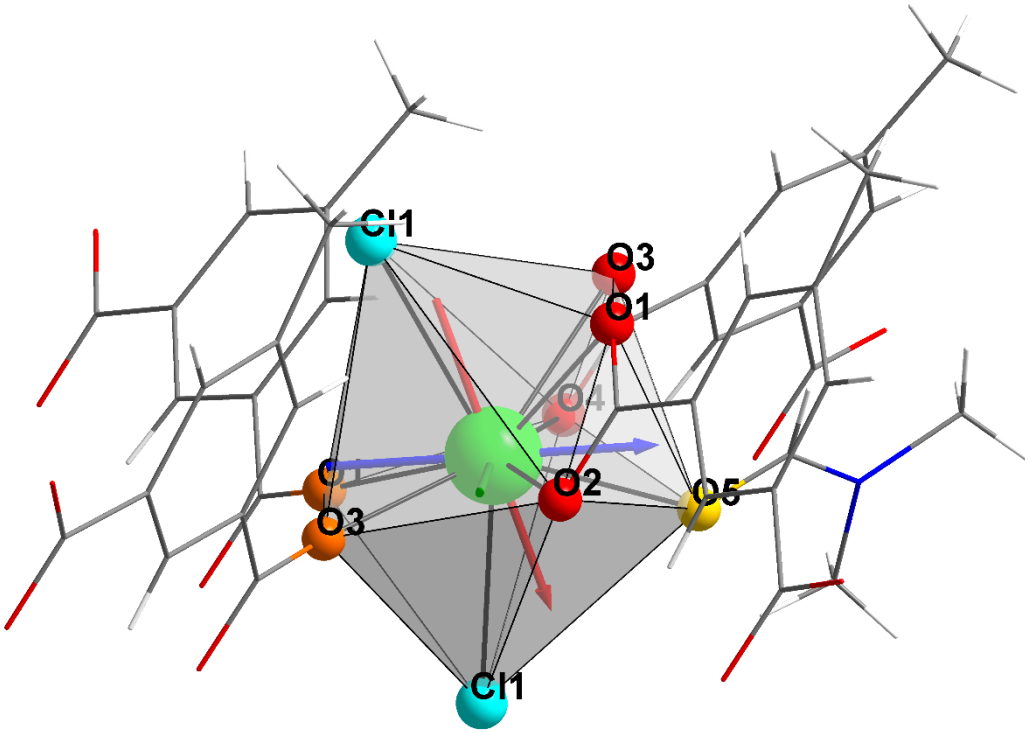

Figure S32. View of the calculated g-tensor for a coordination excerpt of compound **GR-MOF-18**. The longest Ce-O and Ce-Cl bond distances (specifically O1-O4 and Cl1(i) atoms) are arranged in a plane but Cl1 atom is sited out of that plane.

Table S5. Single_Aniso computed energy (cm^{-1}) of the KDs, g-tensor values and their wavefunction composition for **GR-MOF-17**.

KDs	Energy	g_x	g_y	g_z	Angle (º)	Wave function composition
1	0	0.459	0.879	3.752	-	92.8%|±5/2>+3.3%|±3/2>+ 3.9%|±1/2>
2	388.067	0.723	1.069	3.401	6.193	4.6%|±5/2>+64.7%|±3/2>+ 30.7%|±1/2>
3	549.011	0.361	0.641	3.790	3.943	2.6%|±5/2>+32.0%|±3/2>+ 65.4%|±1/2>

Table S6. Single_Aniso computed energy (cm^{-1}) of the KDs, g-tensor values and their wavefunction composition for **GR-MOF-18**.

KDs	Energy	g_x	g_y	g_z	Angle (º)	Wave function composition
1	0	0.438	0.518	3.723	-	89.1%|±5/2>+0.2%|±3/2>+ 10.7%|±1/2>
2	287.486	2.167	2.125	0.927	62.74	5.8%|±5/2>+60.6%|±3/2>+ 33.6%|±1/2>
3	915.605	0.272	0.309	4.283	4.839	5.2%|±5/2>+38.1%|±3/2>+ 55.7%|±1/2>

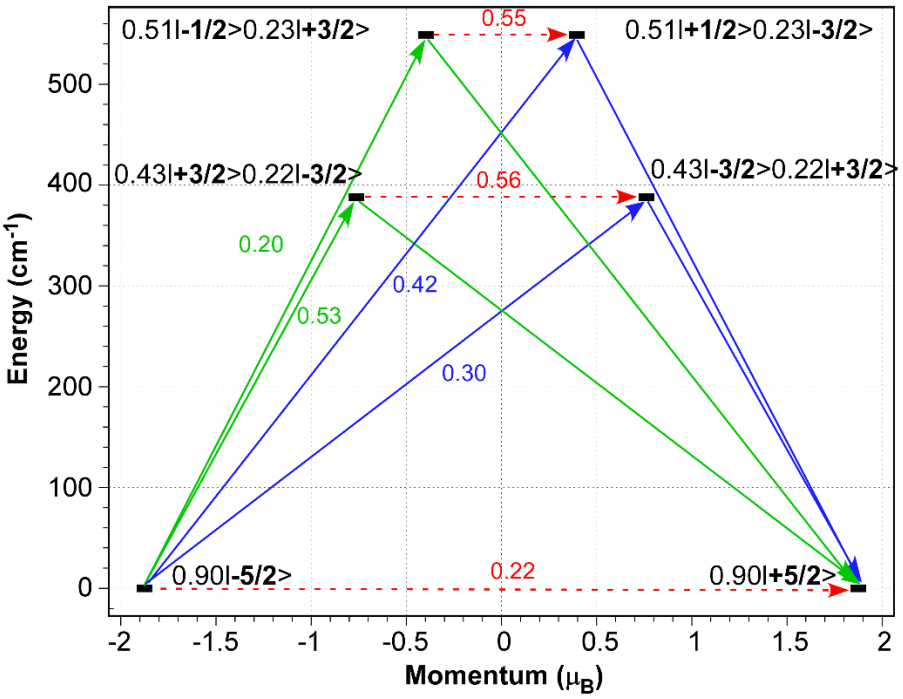

Figure S33. Plot showing the calculated energies for the lowest-lying KDs, their main composition and average matrix elements of the transition magnetic moments (transition probabilities) for **GR-MOF-17**. The red dotted arrows correspond to the quantum tunnelling mechanism of ground and first excited states, while the blue arrow shows the hypothetical Orbach relaxation process. The green arrow indicates the transition between the ground and first Kramers doublets.

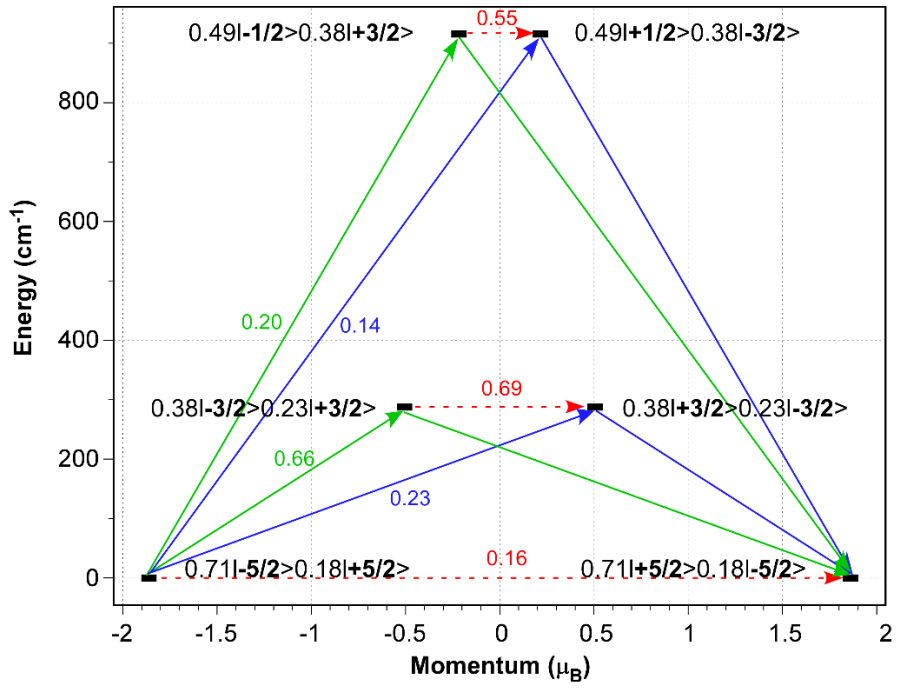

Figure S34. Plot showing the calculated energies for the lowest-lying KDs, their main composition and average matrix elements of the transition magnetic moments (transition probabilities) for **GR-MOF-18**. The red dotted arrows correspond to the quantum tunnelling mechanism of ground and first excited states, while the blue arrow shows the hypothetical Orbach relaxation process. The green arrow indicates the transition between the ground and first Kramers doublets.

S5. Diffuse reflectance spectra.

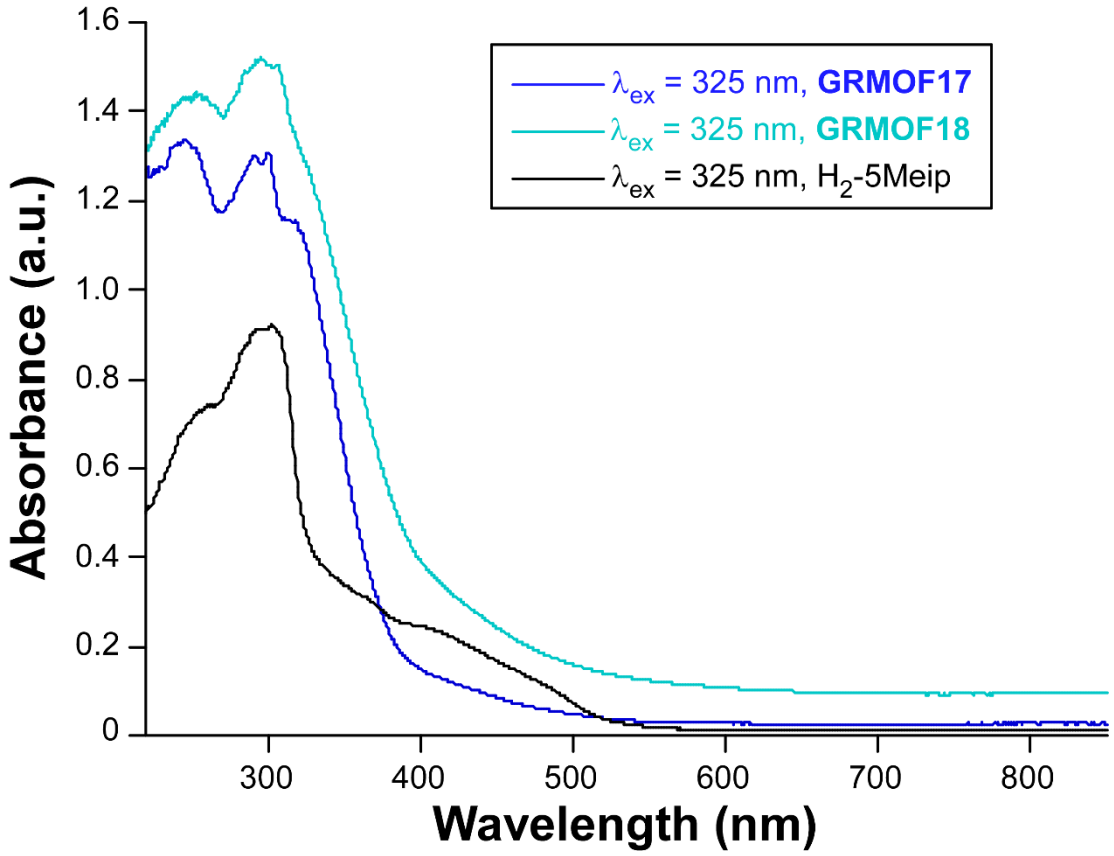

Figure S35. Diffuse reflectance spectra recorded for compounds **GR-MOF-17** and **GR-MOF-18** as well as for the H_2-5Meip ligand at room temperature.

S6. Photoluminescence properties.

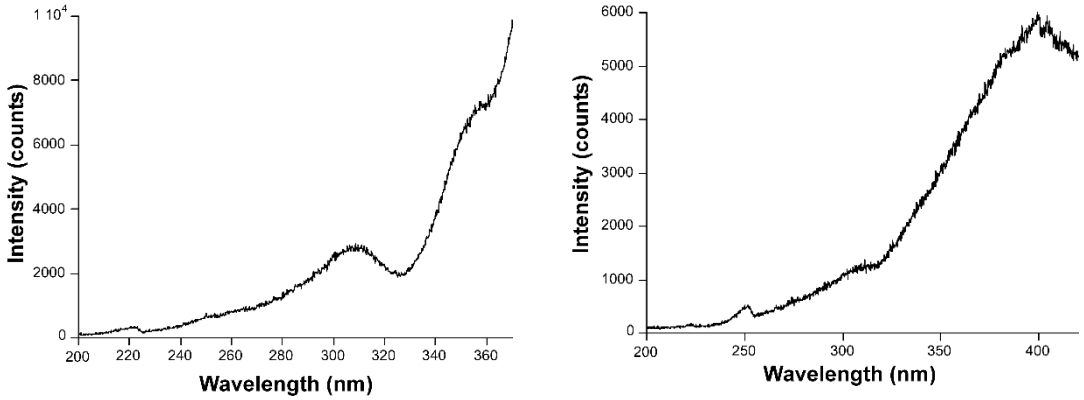

Figure S36. Excitation spectra recorded for the H_2-5Meip ligand at room temperature under variable emission wavelengths: **(a)** λ_{em} = 408 nm and **(b)** λ_{em} = 530 nm.

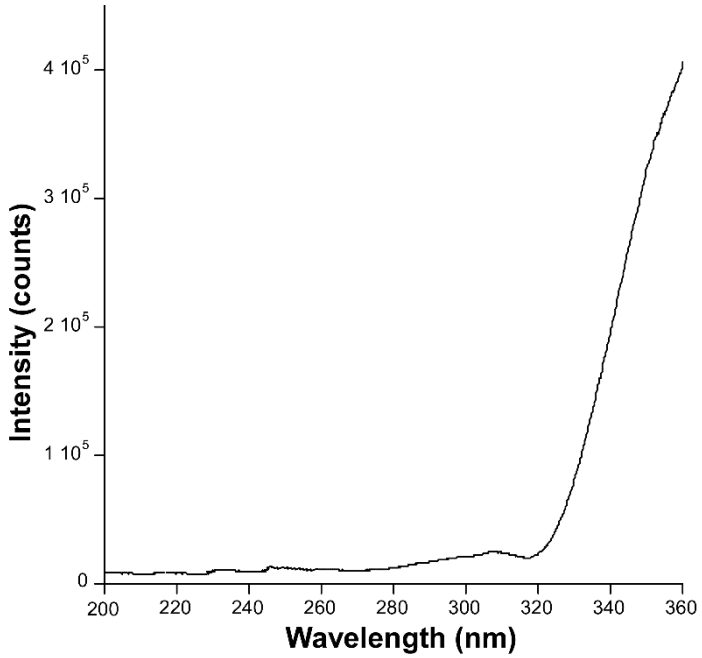

Figure S37. Excitation spectrum recorded for compound **GR-MOF-17** at room temperature at λ_{em} = 397 nm.

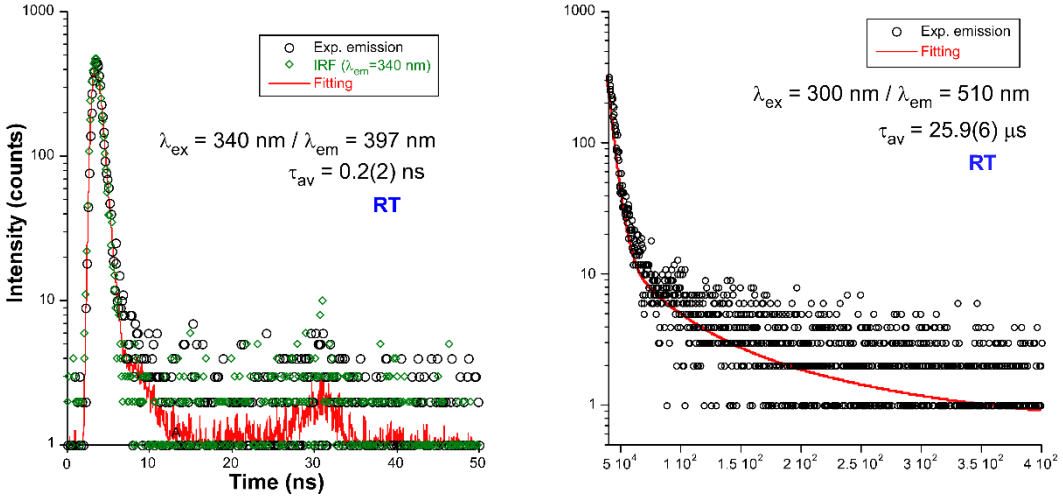

(a) **(b)**

Figure S38. Decay curves showing the best fits for compound **GR-MOF-17** at room temperature at **(a)** λ_{em} = 397 nm and **(b)** λ_{em} = 510 nm.

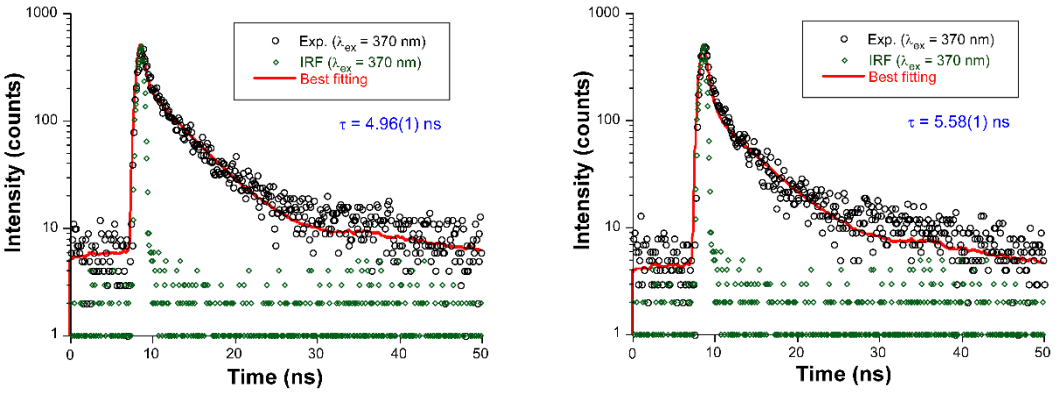

(a) **(b)**

Figure S39. Decay curves showing the best fits for the H_2-5Meip ligand at room temperature at **(a)** λ_{em} = 408 nm and **(b)** λ_{em} = 530 nm.

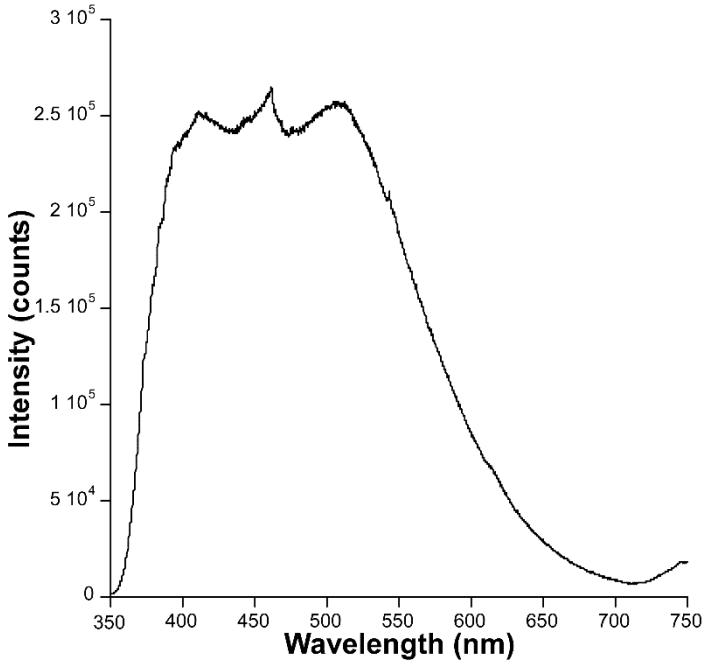

Figure S40. Emission spectrum recorded for compound **GR-MOF-17** at 15 K with λ_{ex} = 325 nm.

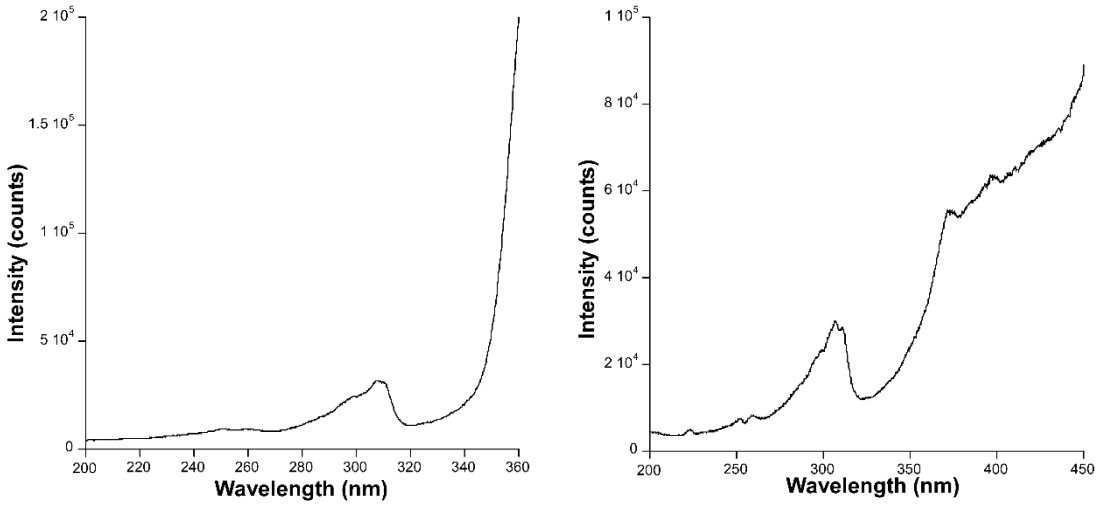

(a) **(b)**

Figure S41. Excitation spectra recorded for compound **GR-MOF-17** at 15 K under variable emission wavelengths: **(a)** λ_{em} = 397 nm and **(b)** λ_{em} = 510 nm.

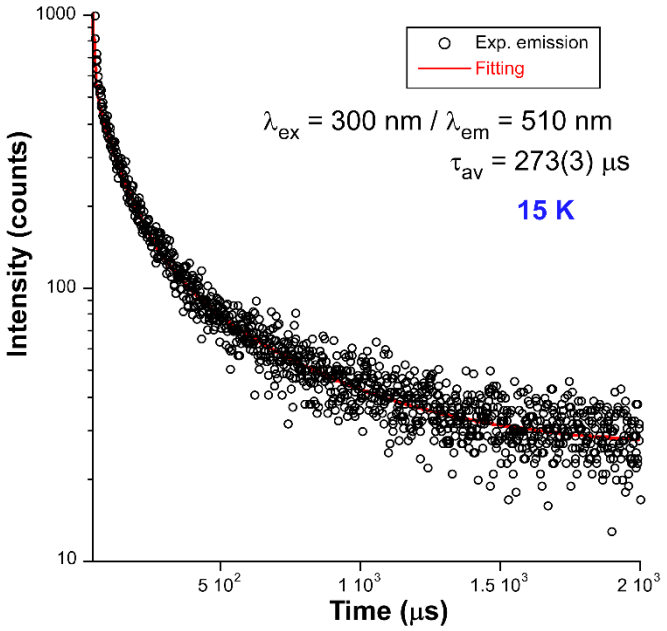

Figure S42. Decay curve showing the best fit for compound **GR-MOF-17** at low temperature for λ_{em} = 510 nm.

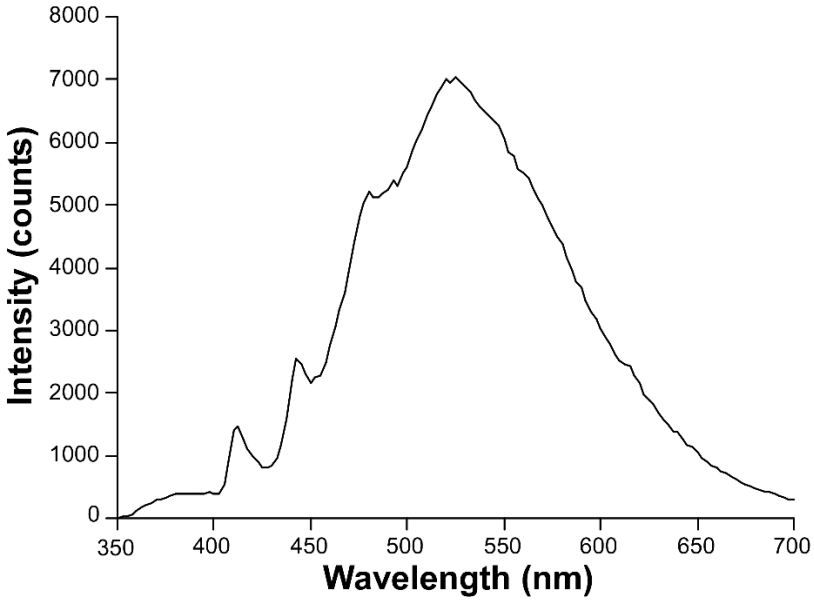

Figure S43. Time-resolved emission spectrum collected with a delay of 50 µs for compound **GR-MOF-17** at 15 K (λ_{ex} = 340 nm).

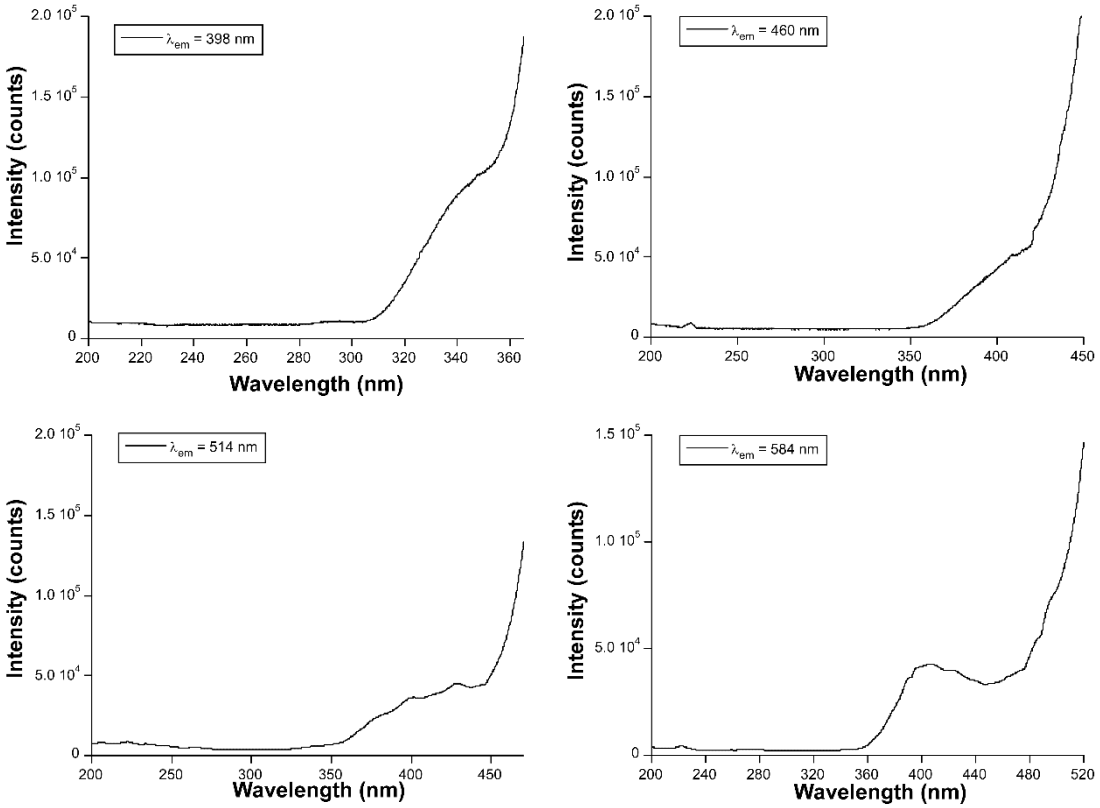

Figure S44. Excitation spectra recorded for compound **GR-MOF-18** at room temperature under variable emission wavelengths (emission bands' maxima).

The decay curves measured at room temperature for **GR-MOF-18** showed a very weak signal with the pulsed LED available that avoided a proper analysis of the lifetime. The emission lifetime could only be recorded for the λ_{em} = 460 and 584 nm emission bands as representative samples. The emission at the first band presents a similar short lifetime of the same order of the free ligand, whereas the second emission band reveals a significantly longer lifetime, which can be associated with an excitation complex formed by the interaction occurring between the aromatic clouds of the DMF and 5Meip ligands (Figure S2).

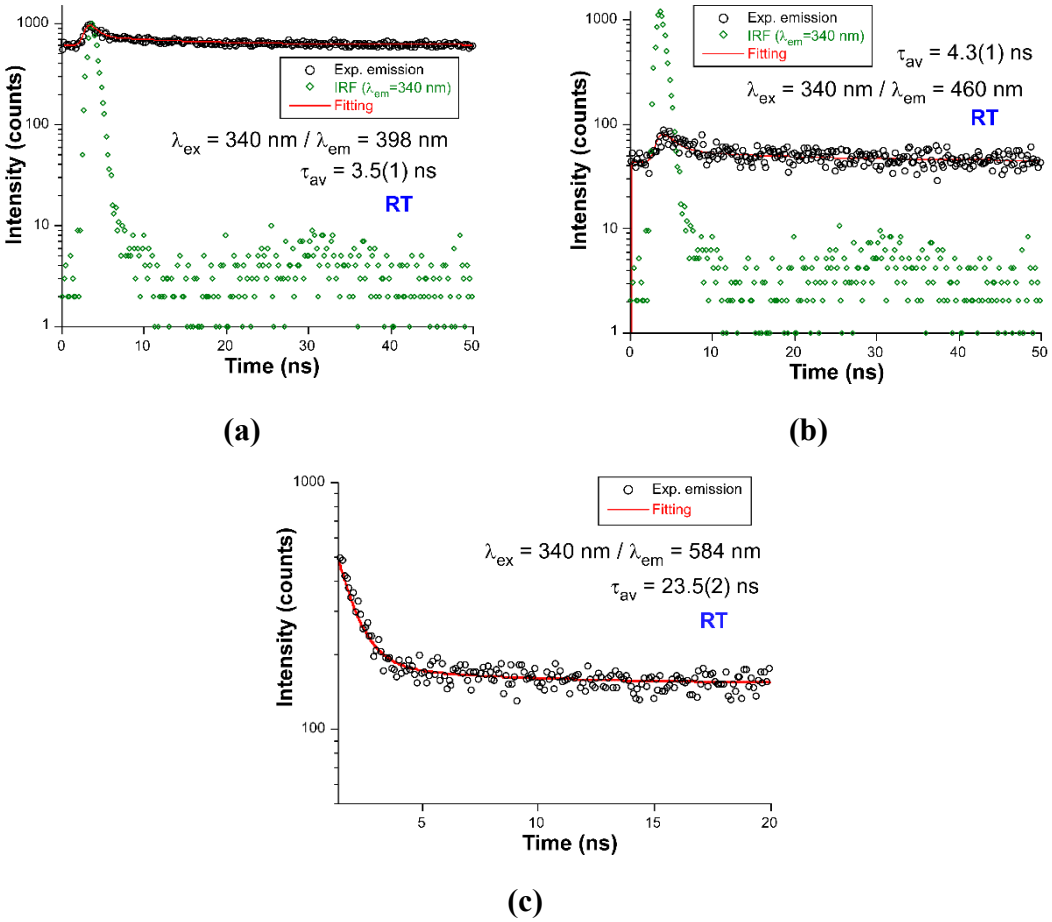

Figure S45. Decay curves showing the best fits for compound **GR-MOF-18** at room temperature at (a) λ_{em} = 398 nm, (b) λ_{em} = 460 nm and (c) λ_{em} = 584 nm.

S6. Powder X-ray diffraction analysis.

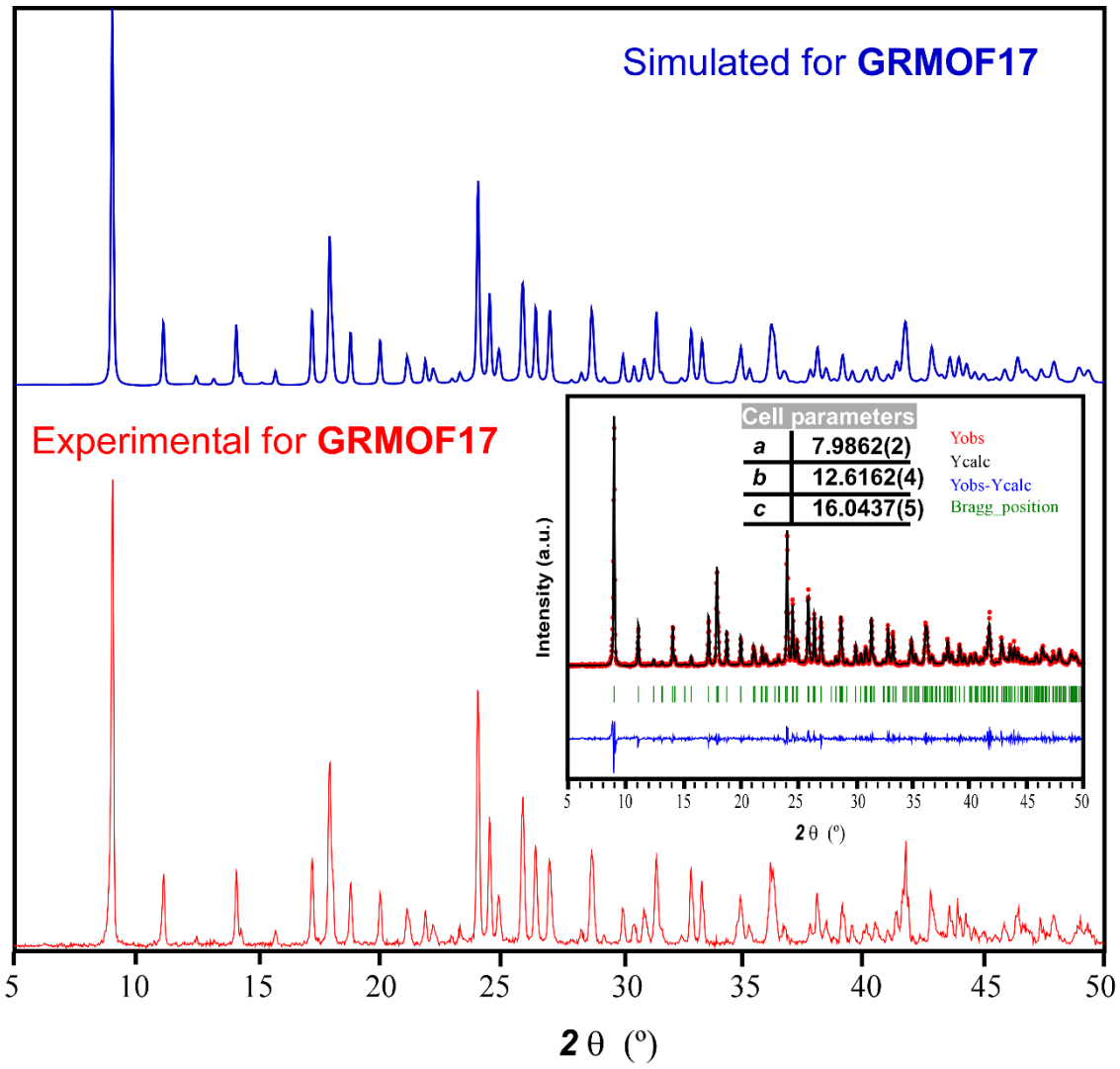

Figure S46. Simulated and experimental PXRD of **GR-MOF-17** with the full profile pattern matching analyses.

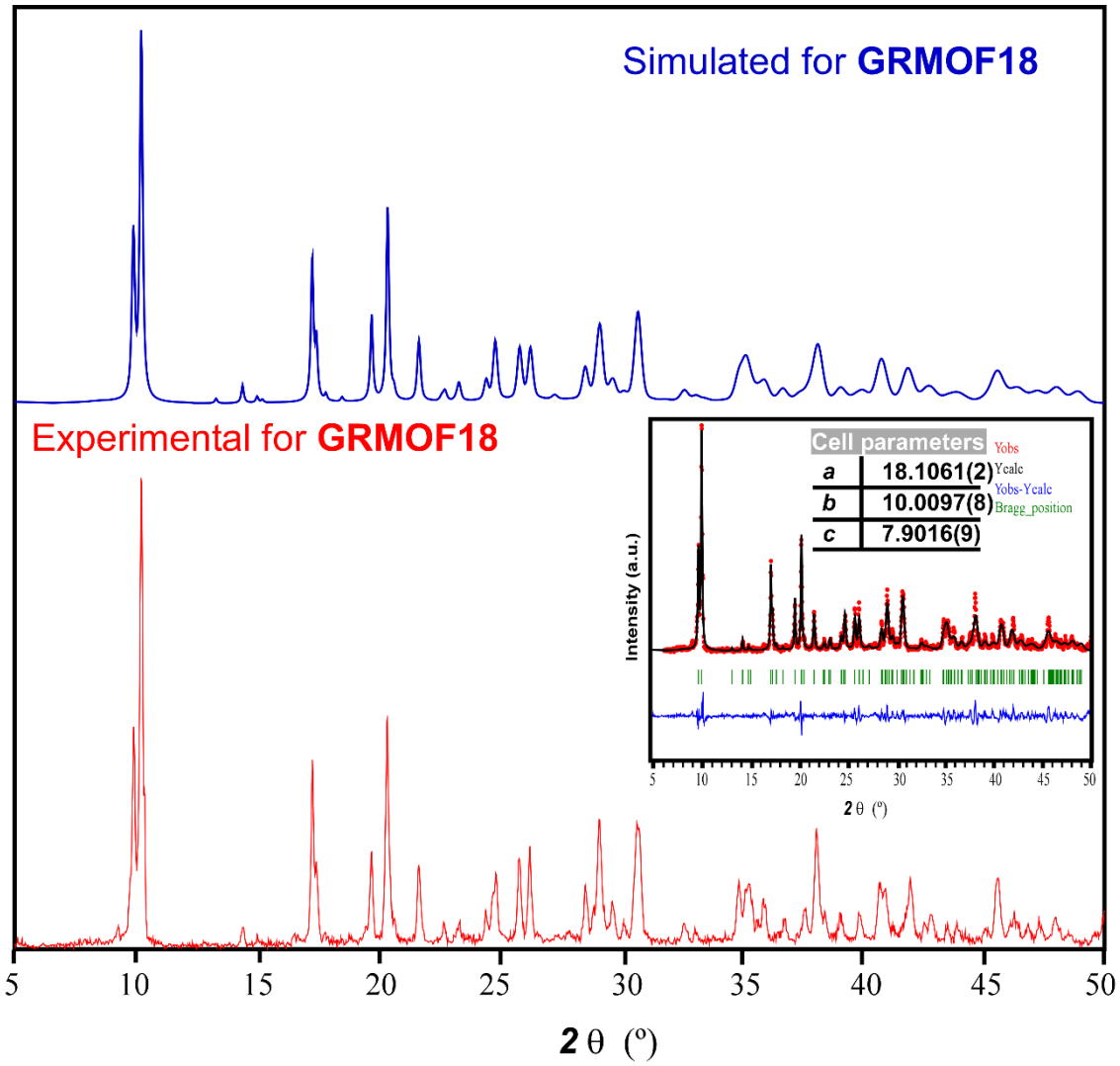

Figure S47. Simulated and experimental PXRD of **GR-MOF-18** with the full profile pattern matching analyses.

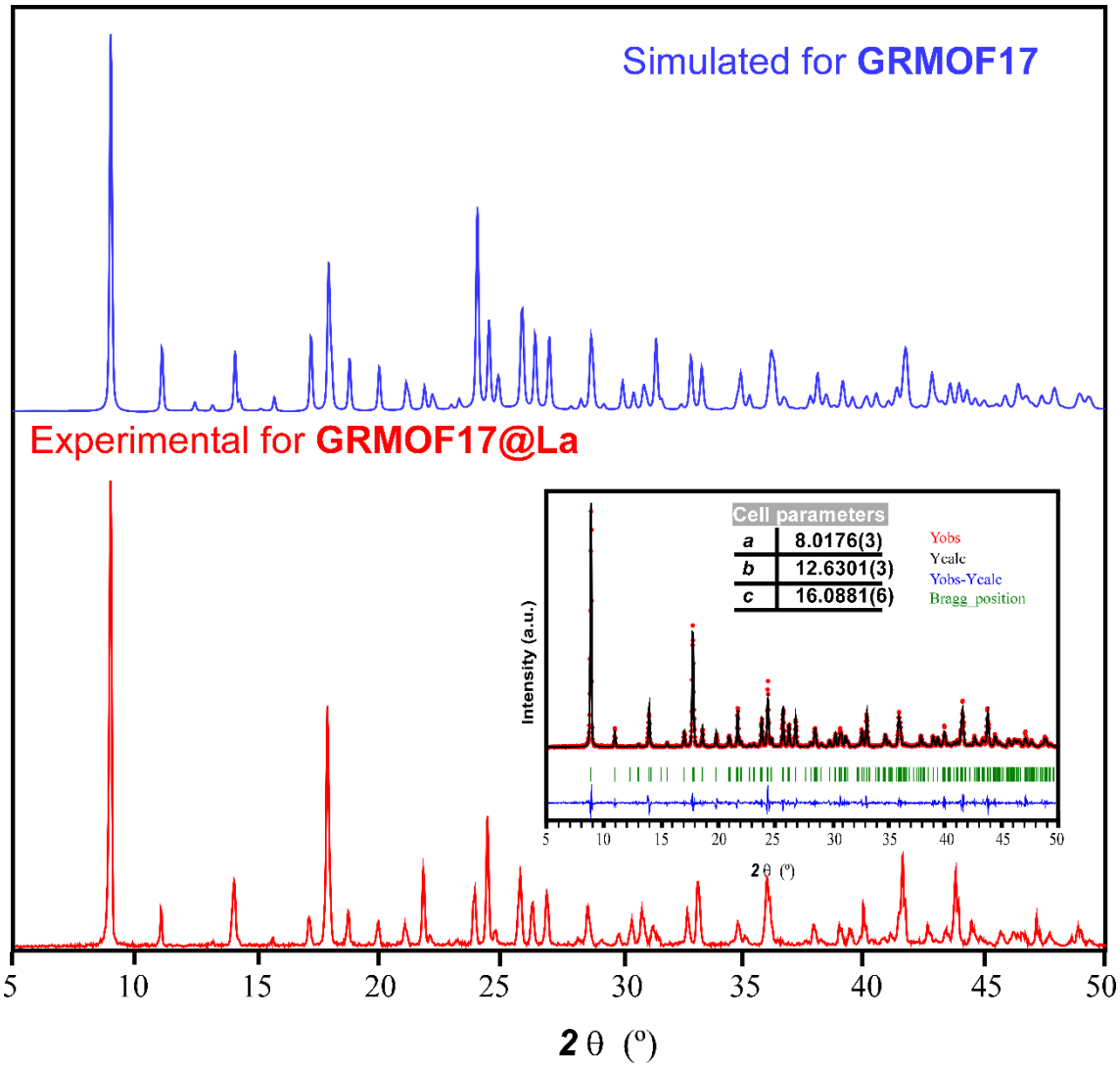

Figure S48. Simulated and experimental PXRD of **GR-MOF-17@La** with the full profile pattern matching analyses.

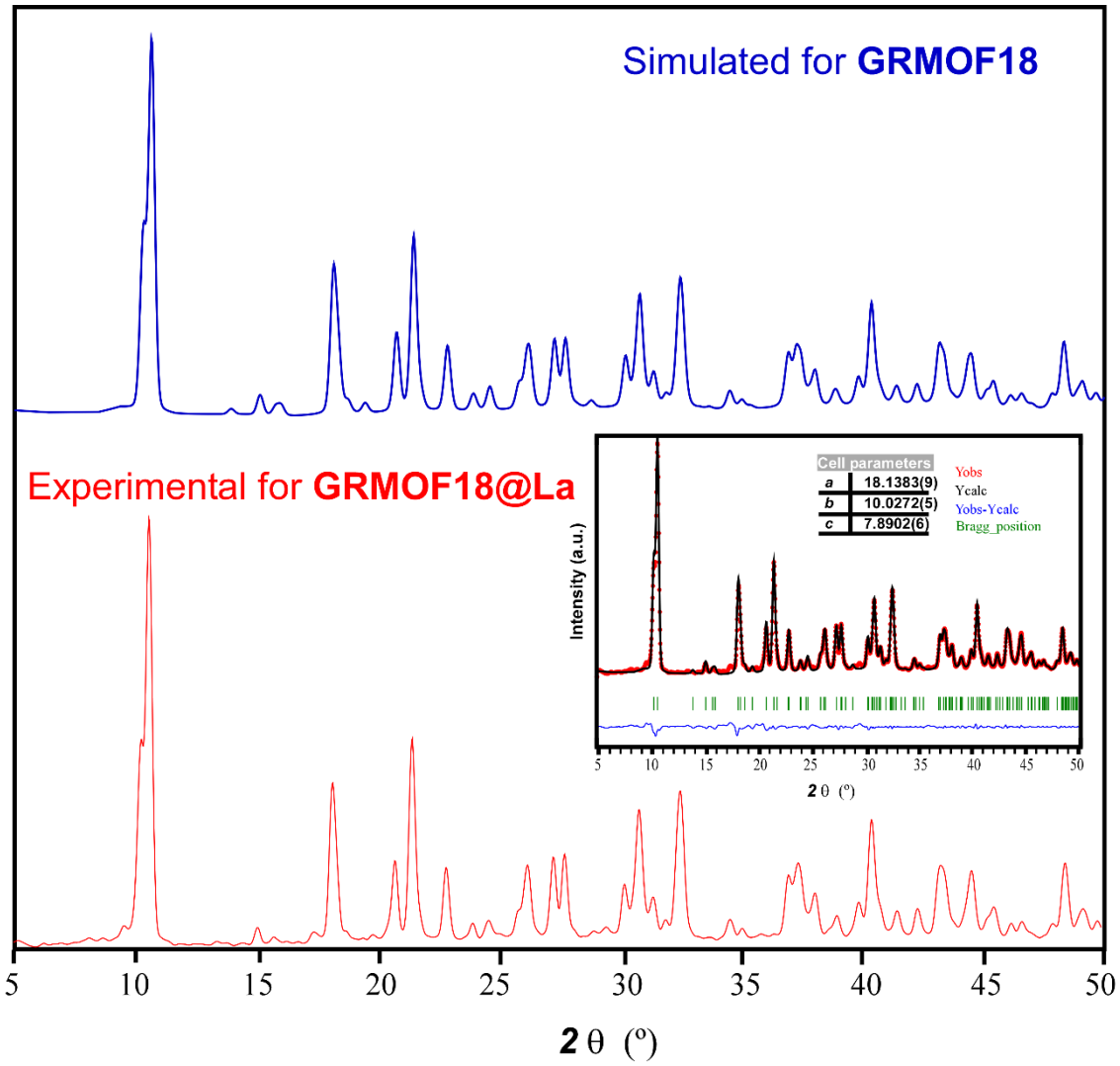

Figure S49. Simulated and experimental PXRD of **GR-MOF-18@La**.